ATOMISTIC SIMULATIONS OF THE VISCOELASTIC RESPONSE

OF A MODEL SINGLE-CRYSTAL EQUIATOMIC SOLID

SOLUTION

A Thesis

by

TUNG YAN LIU

Submitted to the Office of Graduate and Professional Studies of
Texas A&M University
in partial fulfillment of the requirements for the degree of

MASTER OF SCIENCE

Chair of Committee,   Michael Demkowicz
Committee Members,   George M. Pharr IV
                               Amine Benzerga

Head of Department,   Ibrahim Karaman

May 2018

Major Subject: Materials Science and Engineering

ABSTRACT

We use molecular dynamics simulations of cyclic deformation to investigate the viscoelastic response of two-component, defect-free, face-centered cubic equiatomic solid solutions (ESSs). Rather than simulate a specific alloy composition, we use a Lennard-Jones model to study the effect of loading frequency, temperature, model size, and atomic misfit on mechanical energy dissipation. Although free of defects, these models exhibit viscoelastic behavior. We attribute this behavior to the large distortion in the lattice structure induced by atomic misfit. Peaks in loss modulus-frequency plots are due to resonant vibrations occurring at specific frequencies. Moreover, the elastic storage moduli of our ESS models are found to be misfit dependent. Our findings may aid future research in mechanical behavior of concentrated alloys and in molecular dynamics simulations of viscoelastic behavior.

DEDICATION

I dedicated this thesis to my parents, who inspire me to keep learning and stay curious.

ACKNOWLEDGEMENTS

I would like to thank my advisor, Dr. Demkowicz, for his guidance and encouragement throughout the course of this study.

I would also like to thank my committee members, Dr. Pharr and Dr. Benzerga, for their valuable suggestions towards the project. Thanks also go to my friends and colleagues and the department faculty and staff for making my time at Texas A&M University a great experience.

CONTRIBUTORS AND FUNDING SOURCES

NOMENCLATURE

ESS   Equiatomic Solid Solution

Fcc   Face-centered cubic

LAMMPS   Large-scale Atomic/Molecular Massively Parallel Simulator

L-J   Lennard-Jones

MD   Molecular Dynamics

TABLE OF CONTENTS

Page

LIST OF FIGURES

Page

LIST OF TABLES

1. INTRODUCTION

When a defect-free, single crystal metal is strained periodically below its elastic limit, its stress response is time-independent. When the same cyclic deformation is performed on a viscous material like a metallic glass, there exists a time lag between the applied strain and stress response due to the fact that energy is dissipated by small-scale structural changes known as "shear transformations" (or "shear transformation zones": STZs [2, 3]). This time-dependent viscoelastic response is often studied through dynamic mechanical analysis where the storage (energy stored) and loss (energy dissipated) modulus are calculated [4].

Equiatomic solid solutions (ESSs) are single phase materials composed of metal elements in equal or nearly-equal proportions. Since the interatomic bonding energies and bond lengths between different types of elements are different, i.e. there are atomic misfits between atom pairs, atoms are slightly displaced from their "perfect" lattice sites. If the misfit is very large, the structure cannot remain crystalline and becomes amorphous, as in a metallic glass [5]. Unlike amorphous solids, ESS retain their crystalline ordering, but also show a significant degree of distortion across the structure [6] that is not found in single-component crystalline metals and alloys.

A recent atomistic study on a two-component, face centered cubic (fcc) defect-free ESS model system demonstrated that ESSs actually exhibit some mechanical responses that

resemble those of amorphous solids [1]. Upon loading, numerous stress drops are observed in the elastic portion of the stress-strain graph as shown in Figure 1, which are caused by localized shear transformations (LSTs) [7, 8] analogous to the STZs seen in metallic glass [2, 3]. These LSTs correspond to transitions between inherent states, i.e. distinct energy minima (stable lattice configurations) [1]. Figure 2 show a sample of such transitions between two inherent states.
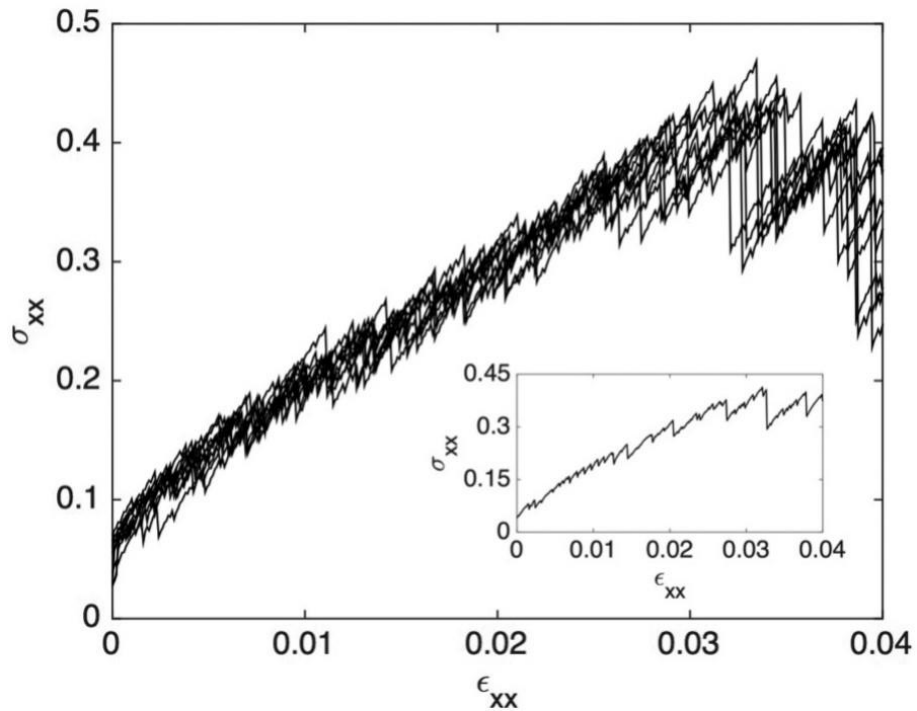
Figure 1: Stack of stress-strain curves where each correspond for loading from one of the ten distinct inherent states found in the structure. The inset displayed one of them. Adapted from [1] with permission.
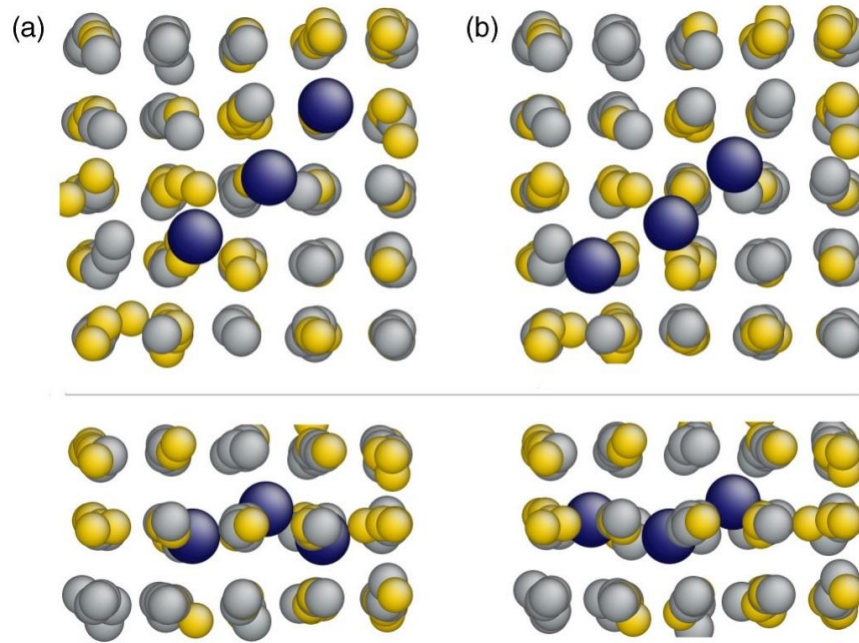
Figure 2: Snapshot of particles (colored in blue) transitioning from one inherent state in column (a) to the other in column (b). Top row is the in-plane view of a {100} plane and bottom row is the edge-on view of it. Adapted from [1] with permission.

While a multiplicity of inherent states is characteristic of amorphous structures [9, 10], it had not been observed in defect-free, single crystal metals before. A plurality of inherent states separated by small energy barriers indicates that ESSs may exhibit a viscoelastic response with greater resemblance to that of metallic glasses, rather than defect-free, single-crystal, single-component metals.

Previous investigations on metallic glasses and composite metals have shown that viscoelastic response may be assessed using atomistic simulations. While many studies have examined factors affecting the strength of ESSs or concentrated alloys [11-14], atomistic modelling of cyclic deformation for the viscoelastic mechanical response of

ESSs has not been studied until 2017 by R. Ranganathan *el at.* [15]. In their paper, the primary focus is to compare the response of three types of structures--- a perfectly ordered alloy, an ESS and an amorphous glass. Therefore, only one misfit is considered for examining the ESS case. In our study, however, we focus on ESSs with different misfits and how that can play a role in their viscoelastic responses.

Although they have shown that ESSs exhibit viscoelastic response in their studies, it remains unclear on the precise mechanism that govern some of the behaviors. For example, a power-law increase in energy dissipation with increasing loading frequencies has been observed [15]. With the aid of the knowledge of ESSs possess inherent states, our study provided insights into explaining such phenomenon, and further extend the scope to how the degree of distortion in ESSs can impact their mechanical responses.

2. METHODOLOGY

2.1 The LJ Model

This proposed study investigates the mechanical response of two-component fcc ESSs under cyclic deformation using atomistic simulations. We investigate how atomic misfit, temperature, and strain rate affect viscoelastic response. Since we are attempting to find general trends in viscoelastic response, the presented work is carried out using binary Lennard-Jones (LJ) systems [16-20] rather than a specific alloy. The interatomic bonding energy between any two LJ particles of type i and j respectively is

$$\phi(r) = 4\epsilon_{ij}[\left(\frac{\sigma_{ij}}{r}\right)^{12} - \left(\frac{\sigma_{ij}}{r}\right)^{6}]$$

where r is the distance between the particle pair, σ_{ij} and ϵ_{ij} are the characteristic bond length and energy between atom type i and j [1]. All the parameters used are presented in LJ units [21].

The structure is built by generating a fcc lattice filled by LJ atom type 1 or 2 randomly with a probability of 0.5. The choice of system is based on that in [1], where $\epsilon_{ij} = 1$ for all pairs, $\sigma_{11} = 1$, $\sigma_{22} = \sigma$ and $\sigma_{12} = \sqrt{\sigma_{11}\sigma_{22}}$. We choose to use the geometric-mean mixing rule for σ_{12} calculation for consistency with study in [1], and this is also one of the standard used in MD simulations [22]. Another commonly used and also the oldest approach [23] is the Lorentz-Berthelot mixing rule [24-26], where the arithmetic mean of the bond lengths is taken instead. The study of mixing rules effect on simulations is

beyond the scope of this paper, but some studies suggest that the Lorentz-Berthelot rule can lead to inaccurate predictions in materials properties [27, 28].

We thus adjust the atomic misfit by using different values for σ, namely, 0.90, 0.88, 0.86, and 0.84. The system is stable in crystalline form for $\sigma \geq 0.84$ [1]. All the simulations are carried out using molecular dynamics (MD) package LAMMPS [22] and the structures are monitored by visualizing snapshots from the simulation using ATOMEYE [29].

2.2 Molecular Dynamics

The essence of the molecular dynamics method is to study movements of atoms by solving classical Newtonian equations of motion for that system of particles interacting through a given potential relation [21] . For classical atomic systems with generalized coordinates q_k, the Lagrangian equation of motion [30] is used

$$\frac{d}{dt}\left(\frac{\partial L}{\partial \dot{q}_k}\right) - \left(\frac{\partial L}{\partial q_k}\right) = 0 \ .$$

$L(q, \dot{q})$ is the Lagrangian, which is just the difference between kinetic (K) and potential energies (V), i.e.

$$L = K - V$$

where for the case of using pair potential,

$$K = \sum_{i=1}^{N} \frac{p_i^2}{2m_i}$$

$$V = \sum_{i=1}^{N-1} \sum_{j=I+1}^{N} \phi(r_{ij})$$

m_i and p_i are the mass and momentum of atom i respectively.

Using Cartesian coordinates r_i, the Lagrangian equation of motion reduces to the familiar Newton second law of motion

$$\boldsymbol{f}_i = m_i \ddot{\boldsymbol{r}}_\iota = m_i \boldsymbol{a}_i$$

Thus, the force on atom i can be calculated by [21]

$$\boldsymbol{f}_i = \boldsymbol{\nabla}_{r_i} L = -\boldsymbol{\nabla}_{r_i} V$$

These forces calculations made MD a relatively time-consuming simulation [31]. Therefore in practice, a cut-off at interatomic distance $r = r_c$ where the interacting forces become negligible is introduced in the potential function, and interacting forces beyond that limit are ignored [21]. In our case, the cut-off of the LJ potential function is taken at $r_c = 2.5\sigma$, where the potential is only 1.6% of the minimum value at $-\epsilon$ [31].

The integration algorithm used in MD simulations is the Verlet algorithm. For a short time interval (defined as a timestep τ) t to $t + \delta t$, the atom trajectories are calculated by performing Taylor expansion about r(t)

$$\boldsymbol{r}(t + \delta t) = \boldsymbol{r}(t) + \boldsymbol{v}(t)\delta t + \frac{1}{2}\boldsymbol{a}(t)\delta t^2 + \cdots$$

$$\boldsymbol{r}(t - \delta t) = \boldsymbol{r}(t) - \boldsymbol{v}(t)\delta t + \frac{1}{2}\boldsymbol{a}(t)\delta t^2 - \cdots$$

And thus their sum gives [21]

$$r(t + \delta t) = 2r(t) - r(t - \delta t) + a(t)\delta t^2$$

In LJ unit, LAMMPS uses $0.005\ \tau^*$ as one time-step (τ), where $\tau^* = \sqrt{\frac{m\sigma^2}{\epsilon}}$.

Physical quantities of interest are calculated and recorded throughout the simulation procedures accordingly. In particular, the temperature of the system is given by the kinetic energy

$$K = \frac{3}{2}Nk_BT$$

and the stress is computed through the pressure of the system [22] by

$$\sigma_{ij} = \frac{\sum_k^N m_k\, v_{ki}v_{kj}}{V} + \frac{\sum_k^N r_{ki}f_{kj}}{V}$$

2.3 Simulation Procedures

Each structure was first relaxed and the system energy is minimized through the conjugate gradient algorithm [32] to ensure the starting configuration is stable. It is then heated up to the desired temperature T in an isobaric ensemble [33] where the pressure in the system was maintained at zero. This procedure ensures that no stresses developed in the material from the thermal expansion before applying any mechanical loading.

After achieving an equilibrium volume at T, cyclic shearing was applied at constant volume. We applied periodically varying tensile and compressive strains along the [100] (x-) direction. Periodic strains of opposite sign are applied along the y-direction so that the volume of the model remains constant. The strain along the z-direction is kept at

zero. The strain profile is sinusoidal in time with a fixed frequency, ω. Each straining period correspond to fifty strain increments. After each strain increment is applied, we let the system dynamically evolve through MD over a specified number of time steps $\Delta\tau$ before applying the next strain increment. The straining process stops after the simulation reaches a total of 5,000,000 time-steps. The frequency ω and number of cycles N completed for each run may therefore be calculated as

$$Frequency\ \omega = \frac{2\pi}{period}$$

$$= \frac{2\pi}{\#\ of\ strain\ increments\ in\ one\ period \times MD\ time\ after\ each\ increment}$$

$$= \frac{2\pi}{50\ \times\ \Delta\tau}$$

$$Total\ number\ of\ completed\ cycles\ N = \frac{total\ time}{period} = \frac{5,000,000}{50\ \times\ \Delta\tau}$$

This loading procedure was used at three different temperatures, four misfit values (mentioned above), and four structure sizes as noted in Table 1. The simulations for different structure sizes are carried out to check if a behavior is an artifact of a model size or a system size-independent material property. All of these parameters are summarized in Table 1, below.

Table 1: Model parameters examined in our simulations.

Parameters	#	Values
Atomic Misfit σ	4	0.84, 0.86, 0.88, 0.90
Loading Frequency ω	46	0.00001-0.025 (the complete set of values and their corresponding $\Delta\tau$ values are attached in the appendix section)
Temperature	3	0.1, 0.2, 0.3
Structure Sizes	4	4000, 8788, 16384, 32000 atoms

2.4 Storage and Loss Modulus Calculations

The stresses recorded in the simulation are used to calculate storage and loss modulus of
the system. In a cyclic deformation, the strain ε, strain rate $\dot{\varepsilon}$ and stress response σ can
be written as

$$\varepsilon(t) = \varepsilon_0 \sin(\omega t)$$

$$\dot{\varepsilon}(t) = \omega \varepsilon_0 \cos(\omega t)$$

$$\sigma(t) = \sigma_0 \sin(\omega t + \delta)$$

where ε_0 and σ_0 is the magnitude of strain and stress respectively, ω is the angular
frequency, t is time and δ is the phase shift angle between the strain and stress. Figure 3
shows an example of applying sinusoidal strain and the corresponding stress response.
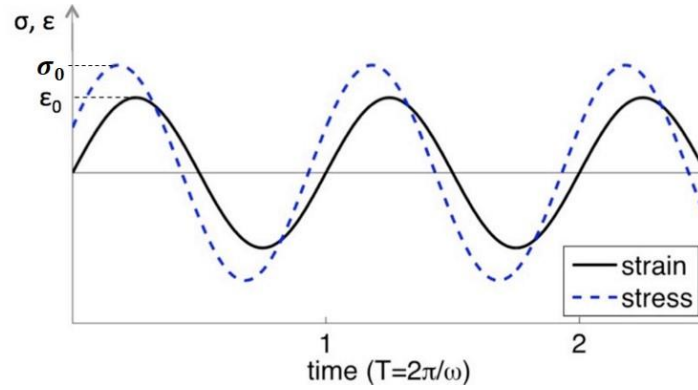
Figure 3: Cyclic deformation and the corresponding stress response with a time lag.

Adapted with permission from [34].

Expanding the sine term in the stress equation, we can define the storage modulus, G_1, and loss modulus, G_2:

$$\sigma(t) = \sigma_0 \cos(\delta) \sin(\omega t) + \sigma_0 \sin(\delta) \cos(\omega t) = \varepsilon_0 G_1 \sin(\omega t) + \varepsilon_0 G_2 \cos(\omega t)$$

where $G_1 = \frac{\sigma_0}{\varepsilon_0} \cos(\delta)$ and $G_2 = \frac{\sigma_0}{\varepsilon_0} \sin(\delta)$.

Storage modulus describe the stored elastic energy in a cycle, while loss modulus represents the energy dissipated per cycle. The averaged dissipated energy can be calculated by integrating the power (work rate) *(24)*

$$\frac{1}{N} \int_0^{N\frac{2\pi}{\omega}} \sigma(t)\dot{\varepsilon}(t) \, dt = \frac{1}{N} \int_0^{N\frac{2\pi}{\omega}} [\varepsilon_0 G_1 \sin(\omega t) + \varepsilon_0 G_2 \cos(\omega t)] \, [\omega \varepsilon_0 \cos(\omega t)] \, dt$$

$$= \pi \varepsilon_0^2 G_2$$

Thus,

$$G_2 = \frac{1}{\pi \varepsilon_0^2 N} \int_0^{N\frac{2\pi}{\omega}} \sigma(t)\dot{\varepsilon}(t)\, dt.$$

Approximating the integral above with a discrete sum, the average loss modulus in our simulations may be calculated by summing over all the data points acquired during cyclic loading as

$$G_2 = \frac{1}{\pi \varepsilon_0^2 N} \sum_{i=1}^{N} \sigma_i \dot{\varepsilon}_i\, \Delta\tau$$

A similar approach may be used to derive an expression for computing G_1:

$$\frac{1}{N}\int_0^{N\frac{2\pi}{\omega}} \sigma(t)\varepsilon(t)\, dt = \frac{1}{N}\int_0^{N\frac{2\pi}{\omega}} [\varepsilon_0 G_1 \sin(\omega t) + \varepsilon_0 G_2 \cos(\omega t)]\,[\varepsilon_0 \sin(\omega t)]\, dt$$

$$= \frac{\pi}{\omega}\varepsilon_0^2 G_1$$

Thus,

$$G_1 = \frac{\omega}{\pi \varepsilon_0^2 N} \sum_{i=1}^{N} \sigma_i \varepsilon_i\, \Delta\tau,$$

where N is the total number of straining cycles carried out in the simulation.

3. RESULTS AND ANALYSIS

3.1 Viscoelastic Responses

3.1.1 Time-Dependent Stress Responses

Instead of giving linear elastic responses, we found that our defect-free ESSs exhibit

viscoelastic responses. Figure 4 shows two examples of the stress-strain curves obtained

for simulations with loading frequency of 0.0209. Both of them have an ellipsoidal

shape, which suggested the presence of energy dissipations during the loading cycles.

Figure 5 and Figure 6 shows the starting four cycles of the red curve in Figure 4.
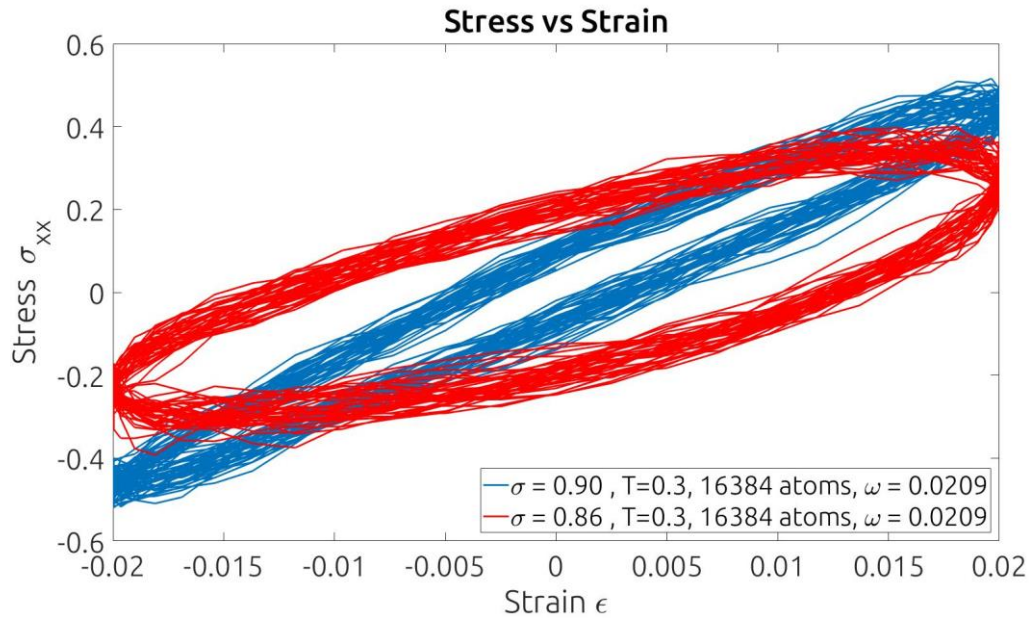
Figure 4: Stress-strain curve correspond to a loading frequency of 0.0209 at T=0.3
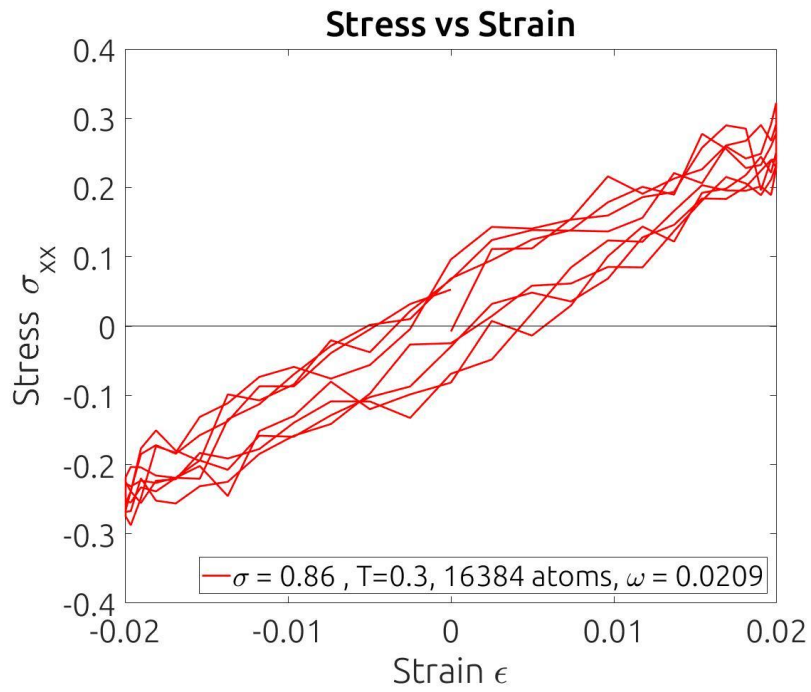
Figure 5: Stress-strain graph of the first four cycles of the red curve in Figure 4
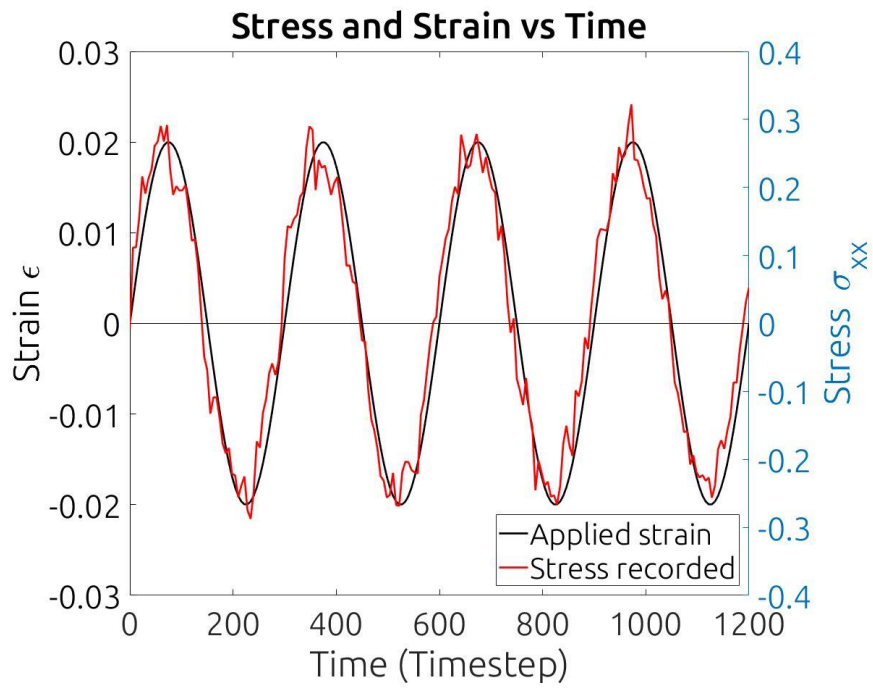
Figure 6: Stress and strain vs time of the first four cycles of the red curve in Figure 4

3.1.2 The Elastic Feature

To verify that ESSs are indeed viscoelastic but not of any visco-plastic nature, we performed cyclic deformation to four ESSs sample with different misfit and stopped deforming the structure after some complete cycles, where the strain is maintained at zero. We then examine how the stress changes with time and found that for all misfits, the stresses decay back to values close to zero within 100 time-steps. Figure 7(a)-(d) shows the stress-time graph we obtained for this examination. We also noticed that there is an "over-shoot" feature in the graph especially for cases with a larger σ value (less distorted structure), but this process only last around 50 time-steps. After the decay period, the oscillation in the stresses around zero is due to thermal fluctuations of the atoms.
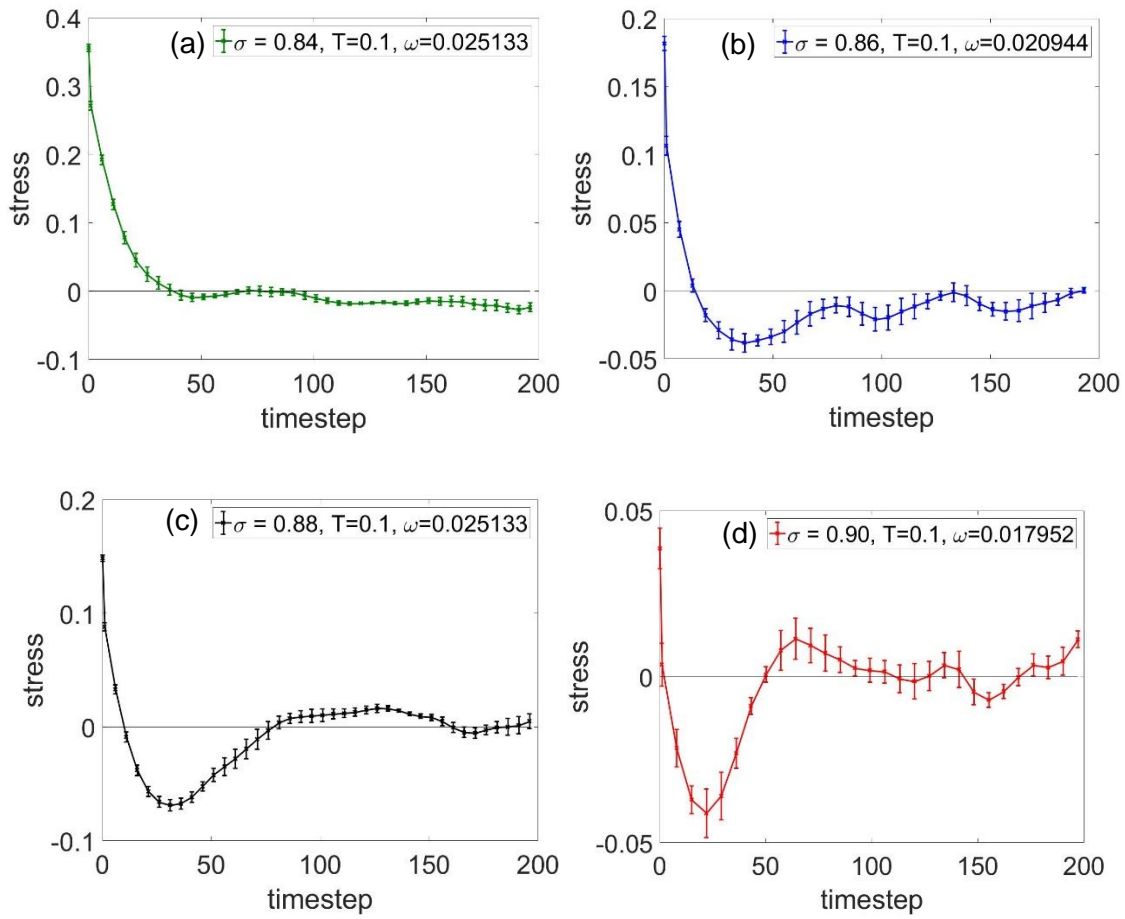
Figure 7: Stress decay over time for structure with different misfit at T=0.1, with (a)

$\sigma = 0.84$, (b) $\sigma = 0.86$, (c) $\sigma = 0.88$ and (d) $\sigma = 0.90$

3.2 Features of Loss Modulus-Frequency Graphs
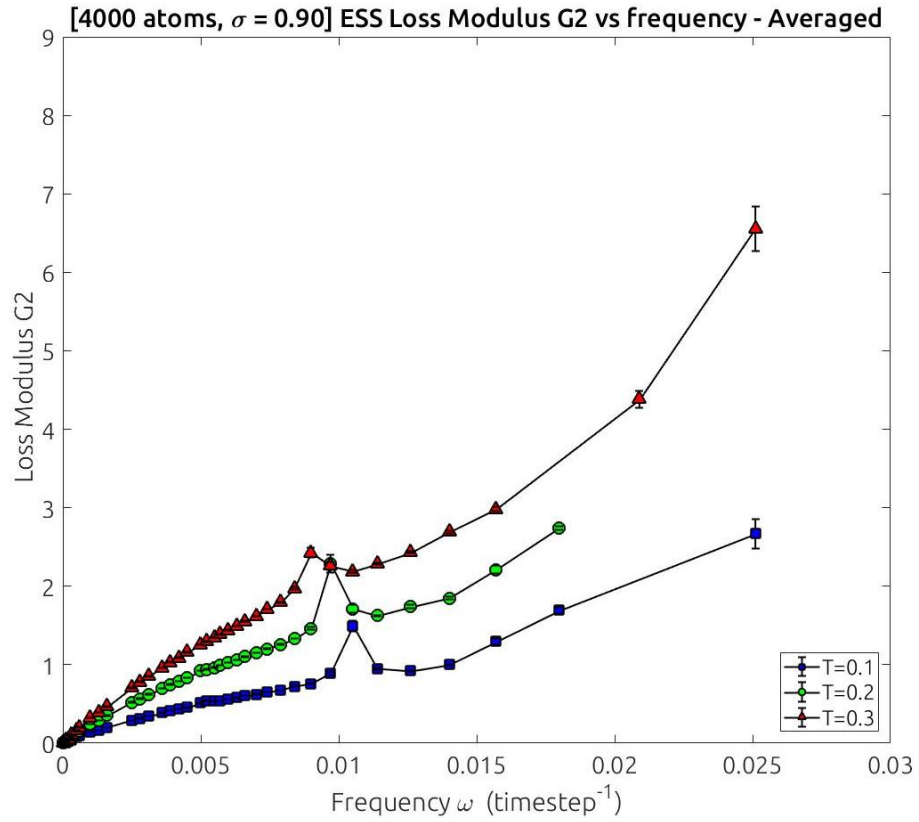
Figure 8: Loss modulus versus frequency for a 4000-atom ESSs system with misfit $\sigma = 0.90$ over three temperatures.
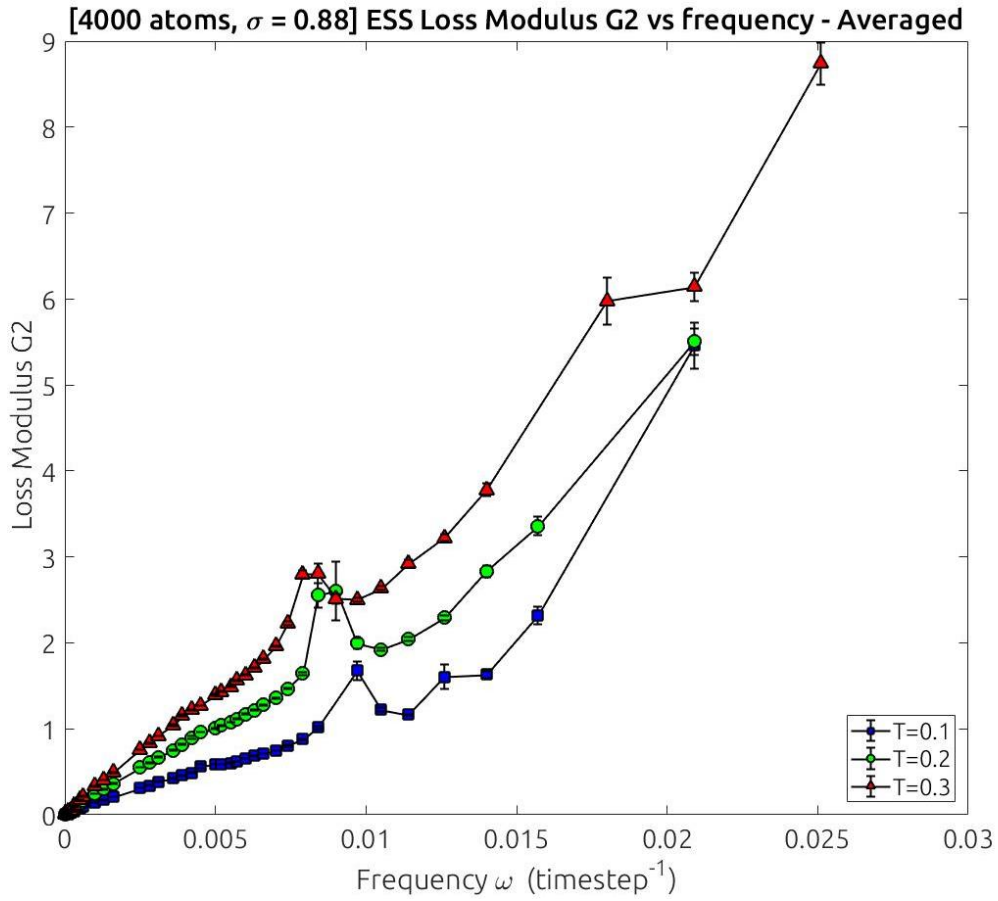
Figure 9: Loss modulus versus frequency for a 4000-atom ESSs system with misfit $\sigma = 0.88$ over three temperatures.

Figure 8 and figure 9 showed the loss modulus-frequency graph for a 4000-atom structure with misfit σ = 0.90 and σ = 0.88 at three temperatures respectively. The figures show two important features. First, there is a general increase in loss modulus as the frequency and temperature increase. The increase with frequency is steeper for higher temperatures. Second, there is a pronounced peak in all of the curves, and the peak shifts to lower frequencies at higher temperatures.
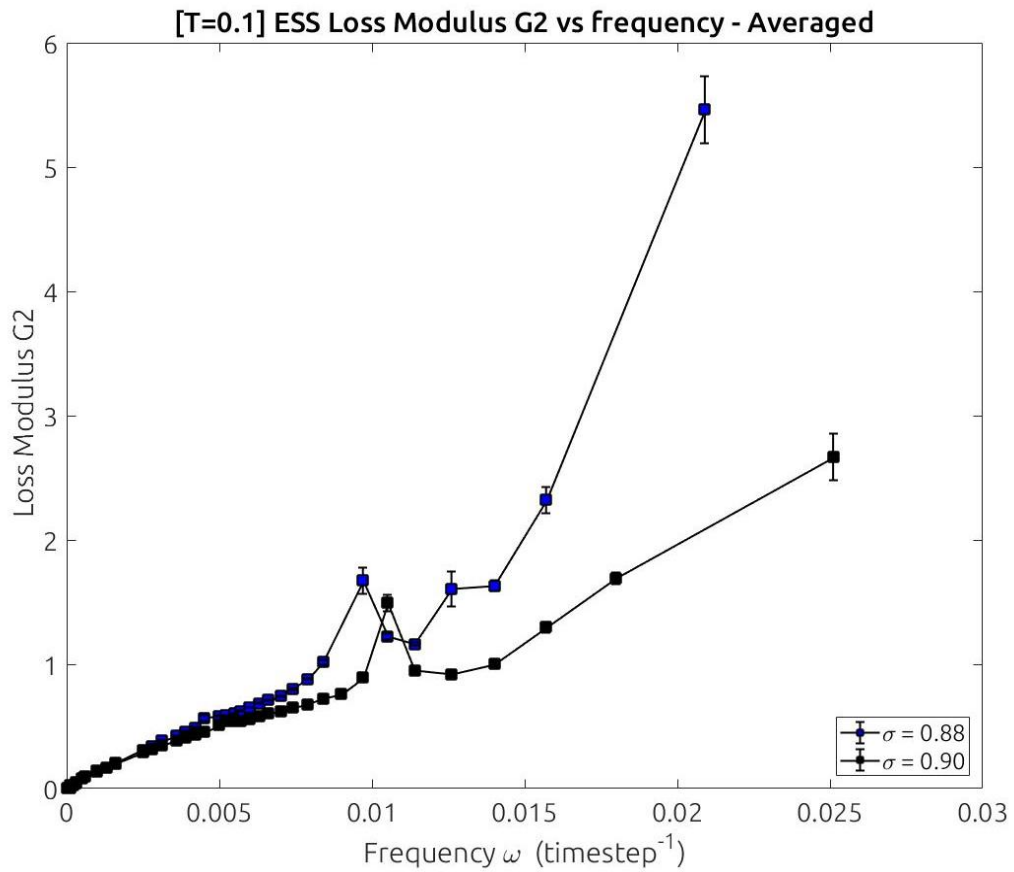
Figure 10: Loss modulus versus frequency curves for the ESSs system with misfit $\sigma = 0.88$ and 0.90 from Figure 3 and 4 at T = 0.1.

Figure 10 shows two curves adapted from figure 3 and 4 that correspond to T=0.1. It appears that the peak is located at a lower frequency for a lower σ value (σ = 0.88), which correspond to a higher misfit, i.e. more severe distortions in the structure. This trend holds for all three temperatures. These loss moduli suggest that the simulated ESS gives a viscoelastic response similar to that of a viscous material, such as a metallic glass.

3.3 The Peaks: Resonant Vibrations

We noticed that the peaks in the loss modulus-frequency graphs shown shift to lower frequencies at higher temperatures. This is contradicting to what is expected for energy dissipation arise from viscoelasticity, for which the peak dissipation should shift to higher loading frequencies as temperature increases. In order to identify the origin of the peaks in the loss modulus-frequency graphs, we check if the frequencies at which the peaks located varies across structure sizes given the same temperature and misfit. Indeed, Figure 11 shows that as the structure sizes increases, the loading frequency corresponding to the first loss modulus peak decreases. This indicated that such feature is not a result from an intensive physical property, and therefore is not associated with the viscoelastic behavior of the material.
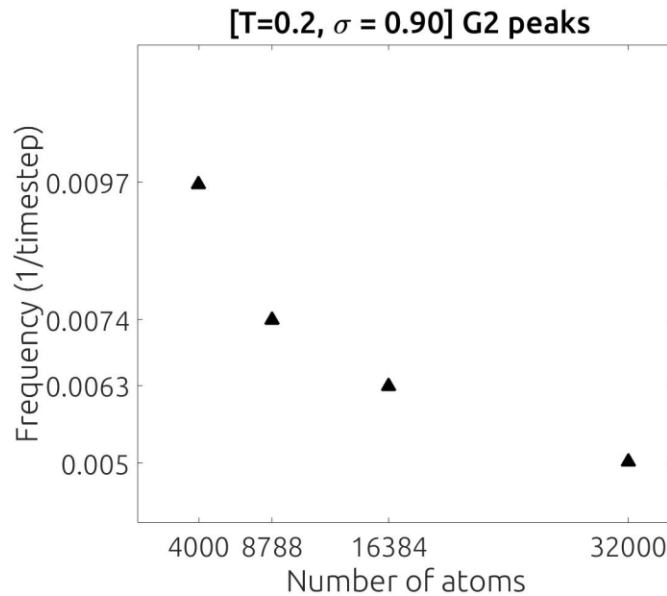
Figure 11: The loading frequencies where the peaks at the loss modulus-frequency graph are located, versus structure sizes in terms of number of atoms.

Apart from the peaks shown in previous figures, there are also peaks with a large

magnitude up to G2=12. We examined the screenshots of the corresponding atomic

structures. We observed special "patterns" at those peaks, illustrated in Figure 12. These

patterns can be found across different temperatures and misfits, but the number of

patterns observed across the loading frequencies for one set of temperature and sigma

decreases with the simulation size. We therefore attribute these peaks with resonant

vibrations. When the loading frequency matches the natural frequency, the material

vibrates in the corresponding vibrational mode, giving rise to the patterns.
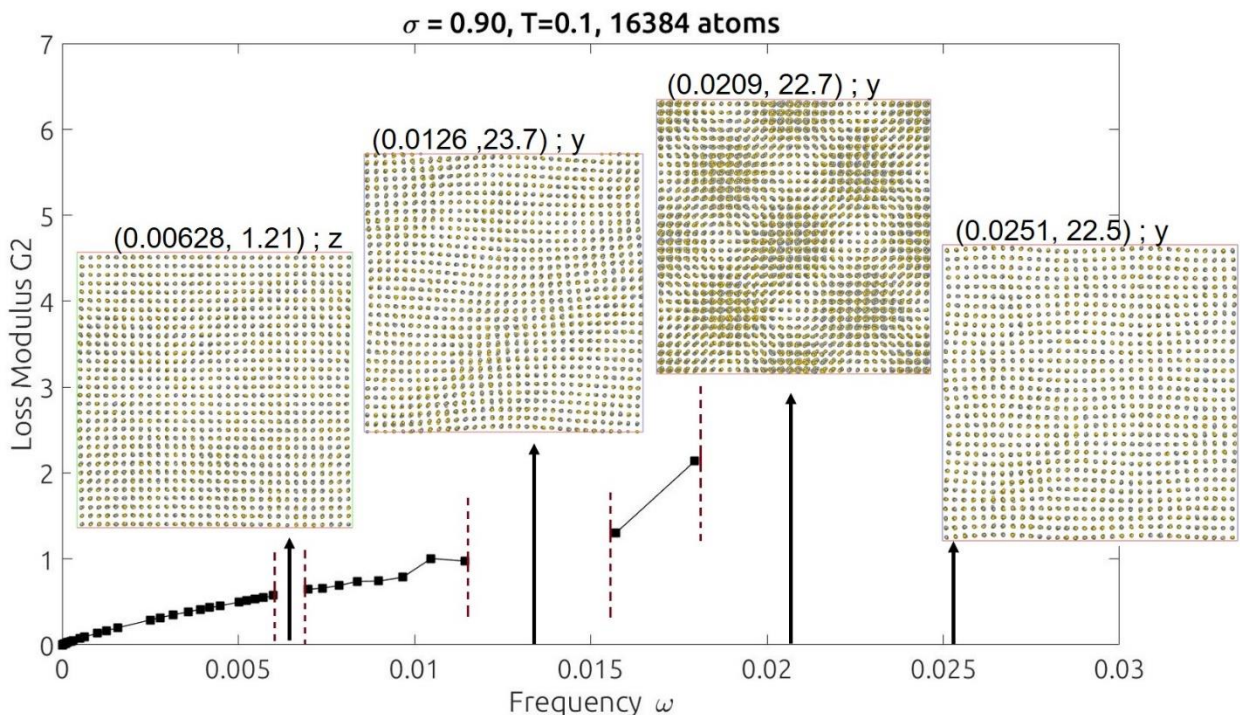
Figure 12: Illustration of observed patterns at loss modulus peaks. Brackets shows

values of (frequency, loss modulus), followed by the direction of point of view.

To illustrate the movement of atoms during these vibrations, we calculated the averaged non-affine displacement of atoms for one set of simulation, where sigma= 0.90, T=0.1. The non-affine displacement is the difference between the location of atoms in a perfect single-component fcc lattice and the location of atoms in the simulation at the same strain ε, thus neglecting the effect of the imposing strain. We then take the average over the total number of atoms, and that gives one non-affine displacement at that time instant. Figure 13 shows that at that particular frequency, the displacement has a sharp increase after around 25 cycles.
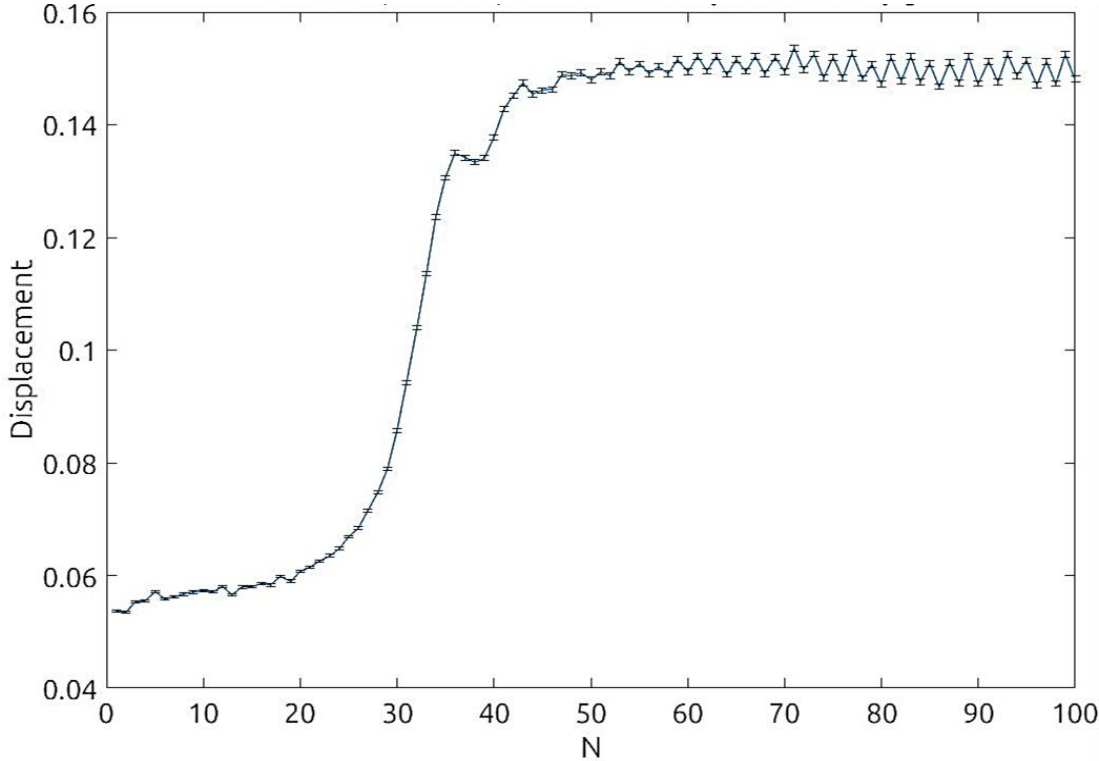
Figure 13: Non-affine displacement versus number of loading cycles

3.3.1 Comparison with the Classical Harmonic Oscillator

The resonant vibration argument presented above can be further understood by examining the harmonic oscillators model and comparing it to our results. Figure 14 shows an illustration of a simple harmonic oscillator.
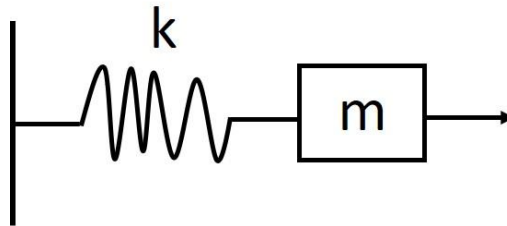
Figure 14: The harmonic oscillator consists of a spring with spring constant k and mass m.

For a simple system comprises of a mass m and a spring with spring constant k, the natural oscillation frequency is just

$$\omega = \sqrt{\frac{k}{m}}$$

If the system is driven at this frequency, resonance occurs. From this relation, it can be deduced that the resonant frequency decreases as the mass increases, or as the spring constant decreases. The spring constant in the model is analogous to the stiffness in a material.

From Figure 11, we have presented that as the number of atoms (which is proportional to the mass of our structure) increases, the frequency corresponding to a peak in the loss modulus-frequency graph decreases. On the other hand, from Figure 8 and 9, the peak shift to lower frequency as temperature increases. For our ESSs, the stiffness, which is proportional to the storage modulus, decreases as temperature increases. This means that as the stiffness decreases, the structure has a lower resonant frequency, which is in agreement with what we see in the harmonic oscillator model.

3.4 The Storage Modulus
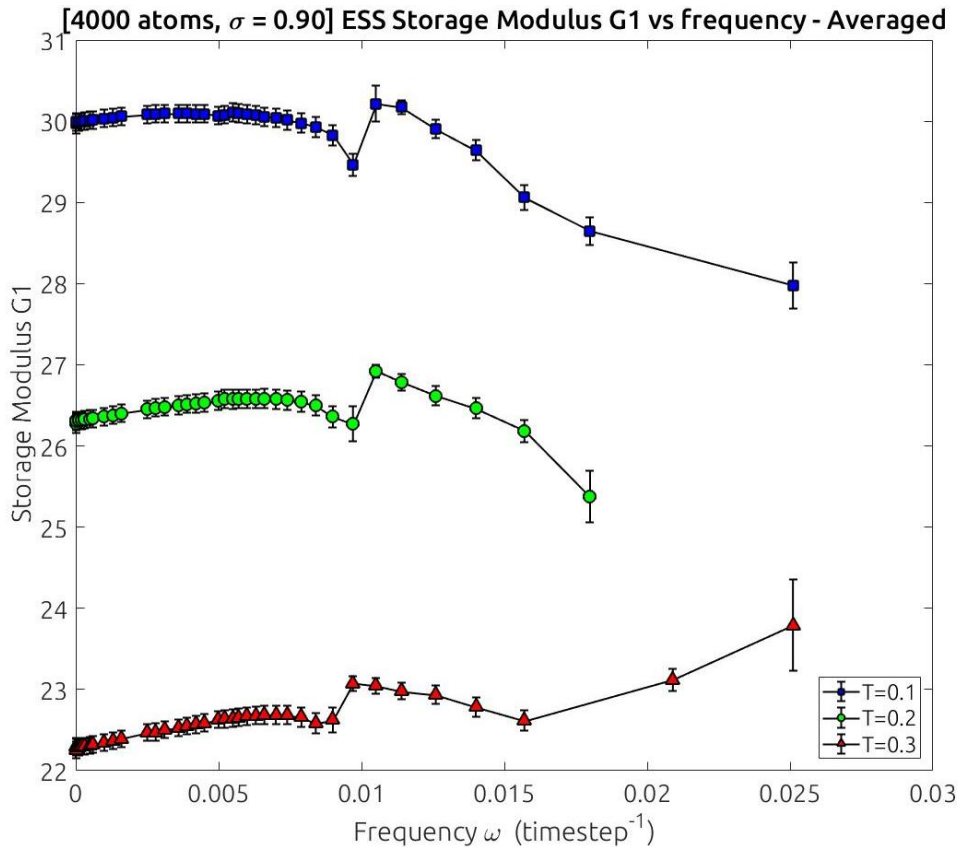
Figure 15: Storage modulus versus frequency for the same system with misfit $\sigma = 0.90$ in Figure 3 over three temperatures.

Figure 15 and 16 shows the storage modulus against angular frequency. For the same structure and temperature condition, the storage modulus maintains a nearly constant value over the range of investigated frequencies. The first "drop" in each of the curves occur near or at the frequency where the peak in the loss modulus graph is located. From both figures, the structure under lower temperature has a higher storage modulus. If we compare the two structures with different misfit at the same temperature, the one with higher σ value (less distorted structure) has a higher storage modulus.
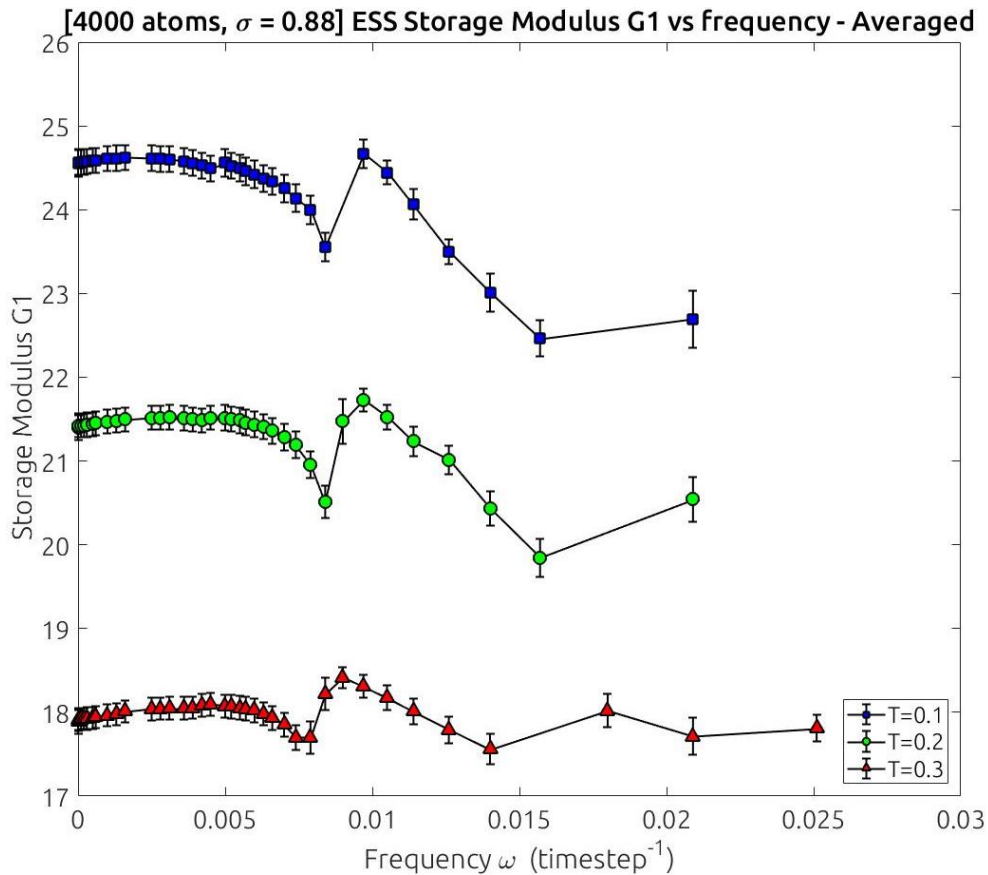
Figure 16: Storage modulus versus frequency for the same system with misfit $\sigma = 0.88$ in Figure 4 over three temperatures.

3.4.1 Modulus Values Not Obeying the Rule of Mixture

In order to compare the storage modulus of structures with different misfits and temperatures, we take the average value of the calculated storage modulus from all the loading frequencies that correspond to a structure with certain misfit and temperature. Figure 17 shows the master graph of the averaged storage modulus versus temperature for all four misfit values of our 4000-atoms ESS structures. Figure 18 is a reference for the G1 values for single component structures with corresponding characteristic bond lengths.
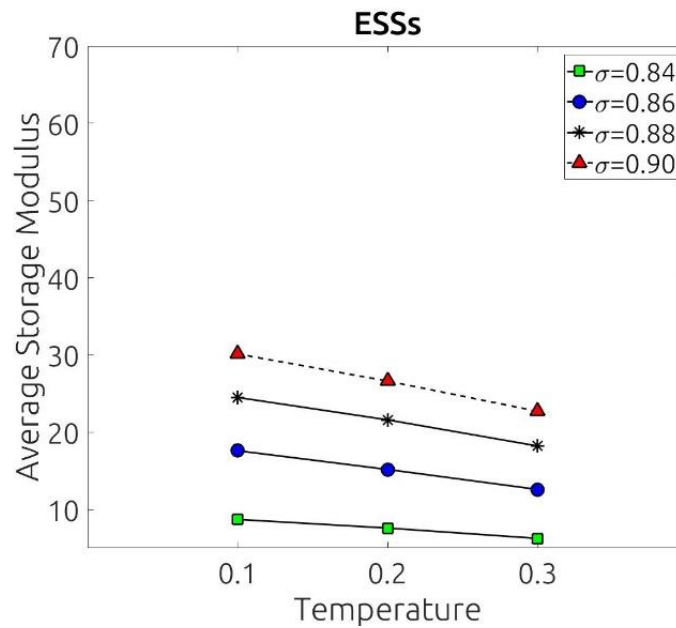
Figure 17: Averaged storage modulus versus temperature for ESSs with varies misfit parameters.
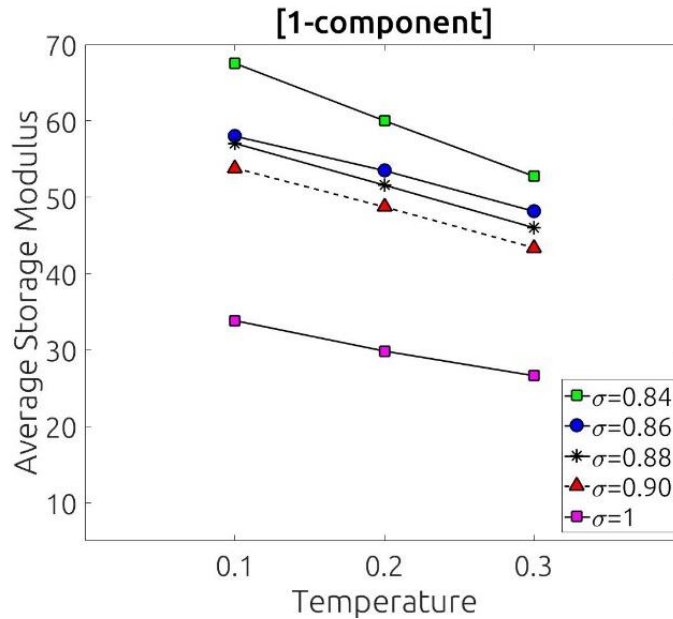
Figure 18: Averaged storage modulus versus temperature for single-component structure with varies characteristic bond length.

As expected, the modulus decreases as temperature increases. When the misfit in the ESSs structure increases (smaller sigma values), the storage modulus decreases. An interesting observation from the storage modulus graphs is that not only does the modulus of ESSs not follow a rule of mixture, the values are way lower than those from the corresponding single-component structure. For example, at T=0.1, the averaged storage modulus of single component with characteristic bond length of $\sigma=1$ and $\sigma=0.84$ are 67.54 and 33.54 respectively, while a ESSs with $\sigma=0.84$ (which correspond to having atom pairs with $\sigma=1$ and $\sigma=0.84$) has an average modulus of 8.70.

3.5 Board Background Increase

Another pronounced feature in our loss modulus-frequency graph is the presence of a background increase in loss modulus as the loading frequency increase. Neglecting the loss modulus peaks, we fit out data with a straight line in a log-log plot according to the following equation in order to compare the degree of the increases. Figure 19 is an illustration of such treatment.

$$\log(G_2) = A\log(\omega) + B$$
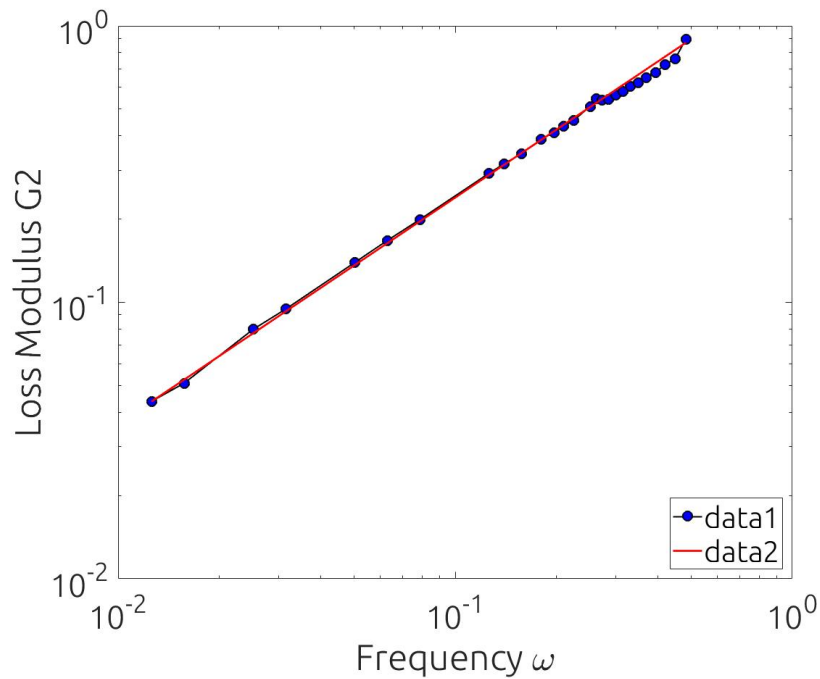
Figure 19: Fitting loss modulus-frequency data in the log-log scale

Figure 20 and 21 shows the fitted slopes (A) and intercepts (B) for our examined structure. The slopes of all data have a value close to 1, while there is a clear trend that

the intercept value increase with decrease misfit values (higher distortion). If we

consider the converted equation

$$G_2 = e^B \omega^A,$$

a higher intercept value corresponds to a larger increase in loss modulus as frequency

increase. This means that the increase in energy dissipation with increasing loading

frequencies is larger in structures that are more distorted.
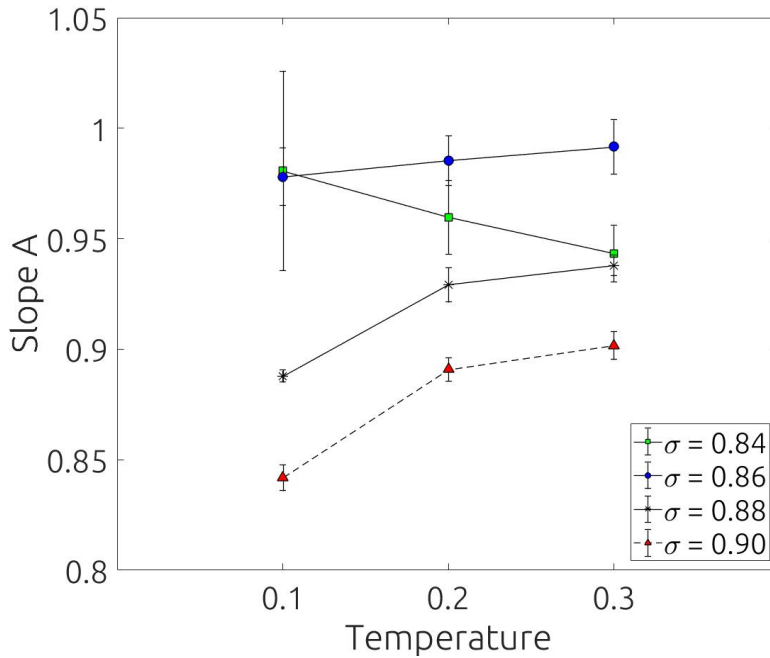
Figure 20: Fitted slopes of loss modulus-frequency data versus temperature for all
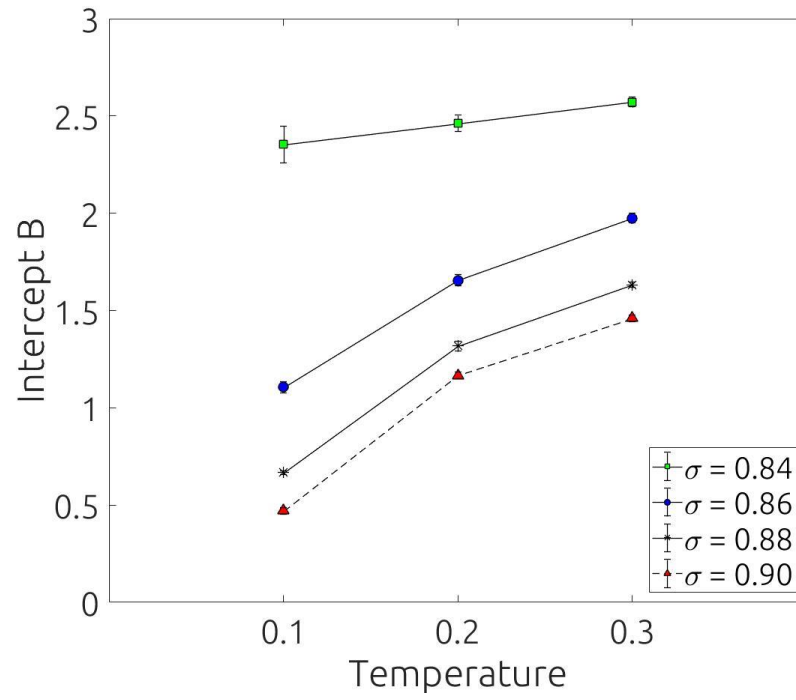
misfits

Figure 21: Fitted intercepts of loss modulus-frequency data versus temperature for all

misfits

4. DISCUSSIONS

4.1 Linear Viscoelasticity and the Standard Solid Model

We made an attempt to understand the viscoelastic behavior observed in the previous section by applying the standard solid model in the scope of linear viscoelasticity. The model consists of a spring connecting with a dashpot in parallel, and another string connecting in series as shown in Figure 22.
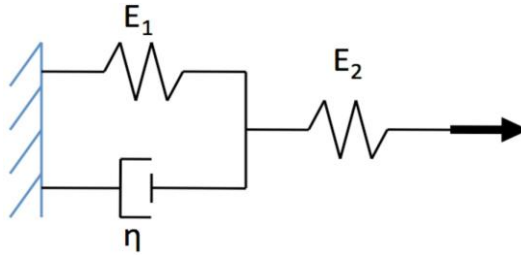
Figure 22: The construction of the standard solid model. Adapted with permission from [34].

The governing equation of motion of this system is given by

$$\frac{E_1}{\eta}\varepsilon + \dot{\varepsilon} = \left(1 + \frac{E_1}{E_2}\right)\frac{\sigma}{\eta} + \frac{\dot{\sigma}}{E_2}$$

where η is the viscosity, E_1 and E_2 are elastic constants. When cyclic motion is applied to the system, the storage and loss modulus can be calculated according by substituting

$$\varepsilon(t) = \varepsilon_0 \sin(\omega t)$$

$$\sigma(t) = \sigma_0 \sin(\omega t + \delta),$$

which gives

$$G_1 = \frac{E_1 E_2 (E_1 + E_2) + E_2 \eta^2 \omega^2}{(E_1 + E_2)^2 + \eta^2 \omega^2}$$

$$G_2 = \frac{E_2{}^2 \eta \omega}{(E_1 + E_2)^2 + \eta^2 \omega^2}$$

Figure 23 and 24 shows examples of storage (G1) and loss (G2) modulus graph as a function of loading frequency for a certain η value.
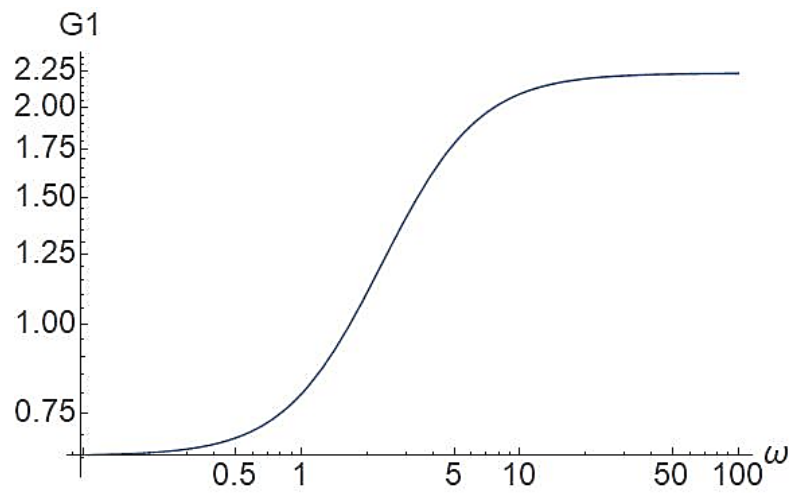
Figure 23: Illustration of storage modulus-frequency relation obtained from the standard solid model
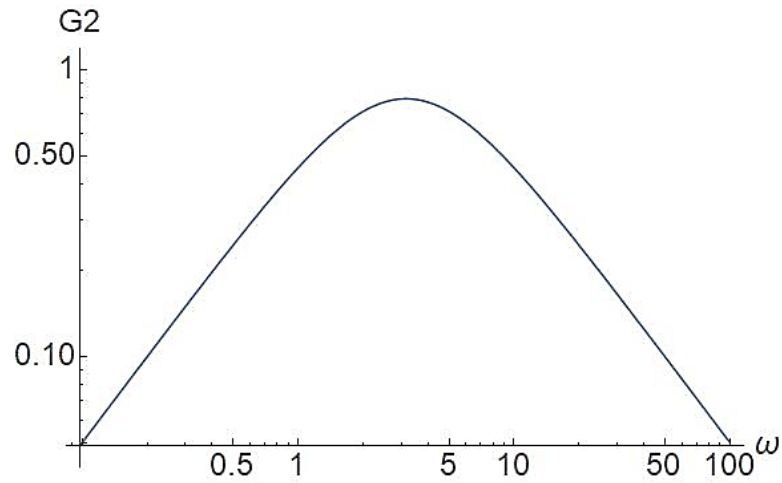
Figure 24: Illustration of loss modulus-frequency relation obtained from the standard solid model

As noted in section 1, ESSs possess of numerous inherent states, which suggest the idea of transitions with different activation energies. We therefore propose that the board background increase in loss modulus-frequency graph may be the result of such transitions, which leads to the idea that at different loading frequencies, the material has different viscosity values. Thus the background increase is the result from adding all corresponding loss modulus peaks (as shown in Figure 24) across the span of the loading frequencies. This idea is demonstrated in Figure 25.
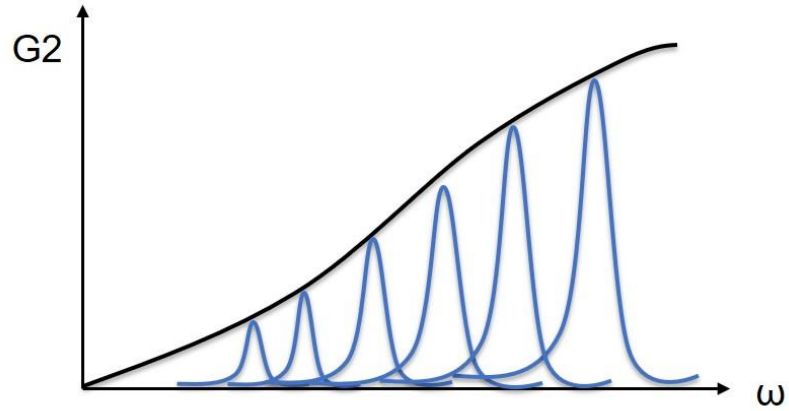
Figure 25: Illustration of the idea that ESSs possess different viscosity across different loading frequencies.

4.2 Fitting the Loss Modulus-Frequency Data

To examine this hypothesis, we employ the idea to our data by calculating the expected loss modulus and fit the relation to our data.

$$G_2(w) = \int_0^\infty f(\eta) G_2^{ss}(\eta, w) \ d\eta$$

$$f(\eta) = 2\gamma(T)\eta \ e^{-\gamma(T)\eta^2}$$

$$G_2^{ss} = \frac{\alpha \ \eta\omega}{\beta + \eta^2\omega^2}$$

$f(\eta)$ is the distribution of viscosities, where $\gamma(T)$ is a parameter that account for the temperature dependence. G_2^{ss} is the same loss modulus relation from the standard model, with the fitting parameters α and β defined by

$$\alpha = E_2{}^2$$

$$\beta = (E_1 + E_2)^2$$

The integral gives

$$G_2 = \frac{\alpha\gamma}{\omega^3}\left\{\omega^2\sqrt{\frac{\pi}{\gamma}} + \pi\omega\sqrt{\beta}e^{\frac{\beta\gamma}{\omega^2}}[Erf\left(\frac{\sqrt{\beta\gamma}}{\omega}\right) - 1]\right\}$$

Figure 26 shows an example of a best fit obtained. Although the model does not fit perfectly to the data, it gives the same trend that the loss modulus increases with loading frequency.
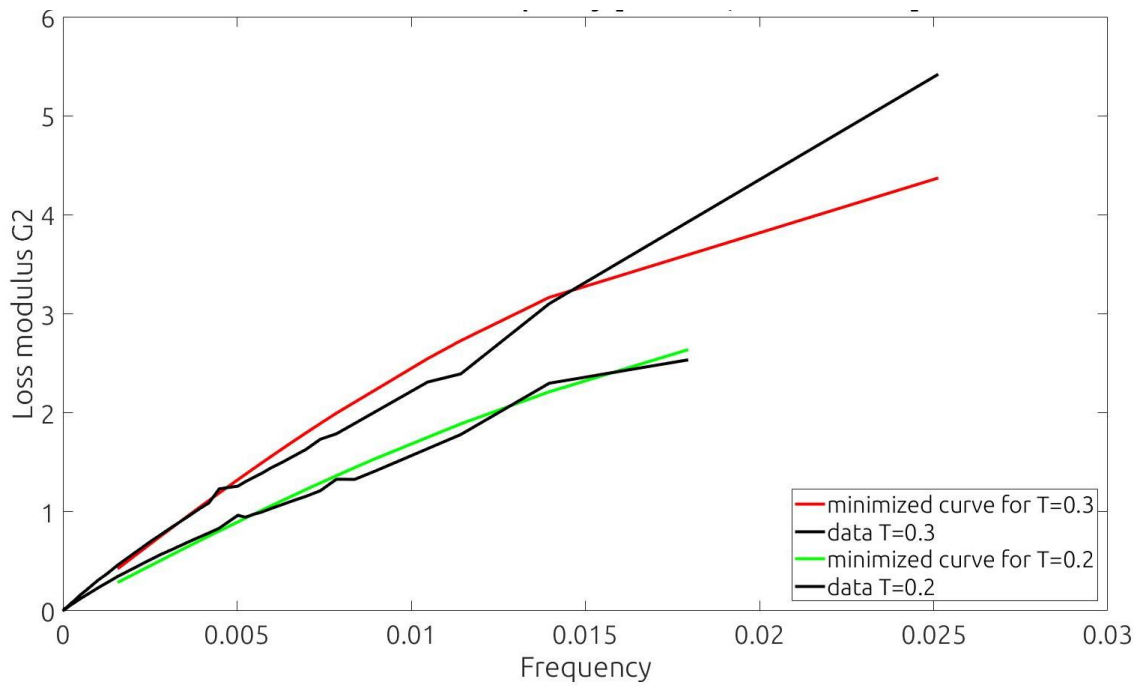
Figure 26: Attempt for fitting the loss modulus using relations based on the standard solid model

We then used the fitted parameters α and β to calculate the corresponding storage modulus values in order to further verify if the hypothesis works. The storage modulus can be obtained using the same method with G1 replacing G2 in the equation

$$G_1(w) = \int_0^\infty f(\eta) G_1^{ss}(\eta, w) \; d\eta$$

$$G_1 = \frac{\sqrt{\alpha\beta}(\sqrt{\beta} - \sqrt{\alpha}) + \sqrt{\alpha}\eta^2\omega^2}{\beta + \eta^2\omega^2}$$

Figure 27 shows the calculated storage modulus, for which the values are negative. Not only are the values off from our storage modulus data, a negative modulus value is not physical.
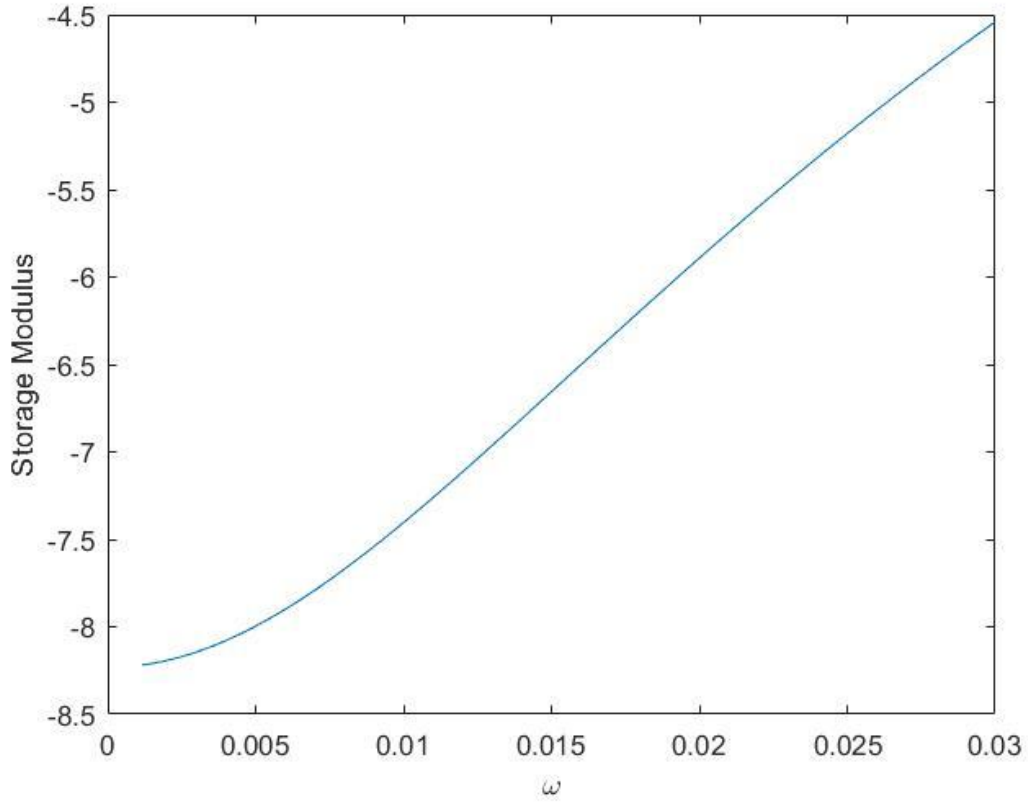
Figure 27: The calculated storage modulus using fitted parameters obtained from loss modulus calculation by applying the standard solid model

4.3 Fitting the Storage Modulus-Frequency Data

Since the fitting mentioned in the previous section is not successful, we tried to do the same process backwards--- first finding the best fit for the storage modulus-frequency data, then uses the fitted parameters to calculate the corresponding loss modulus values.

$$G_1(w) = \int_0^\infty f(\eta) G_1^{ss}(\eta, w) \ d\eta$$

Recall that G_1^{ss} is

$$G_1^{ss} = \frac{E_1 E_2 (E_1 + E_2) + E_2 \eta^2 \omega^2}{(E_1 + E_2)^2 + \eta^2 \omega^2}$$

And the integral gives us

$$G_1 = E_2 - \frac{e^C E_2^2 \gamma (E_1 + E_2) \int_C^\infty \frac{e^{-t}}{t} dt}{\omega^2}$$

where

$$C = \frac{\gamma (E_1 + E_2)^2}{\omega^2}$$

We re-define the parameters, α' and β', as follow

$$\alpha' = E_2$$

$$\beta' = E_1 + E_2$$

so that

$$G_1 = E_2 - \frac{e^C E_2^2 \gamma (E_1 + E_2) \int_C^\infty \frac{e^{-t}}{t} dt}{\omega^2} = \alpha' - \frac{e^{\frac{\gamma \beta'^2}{\omega^2}} \alpha'^2 \gamma \beta' \int_{\frac{\gamma \beta'^2}{\omega^2}}^\infty \frac{e^{-t}}{t} dt}{\omega^2}$$

Figure 28(a)-(b) shows best fits of storage modulus obtained using the same data set as section 4.2. While we can get a fitted curve with values close to our storage modulus data, the curve suggests a decrease in storage modulus as loading frequency increases, rather than the trend we saw in our data.

We finish our analysis by using the fitted α' and β' values to calculate the corresponding loss modulus values, and the results are shown in Figure 29(a)-(b). Since the best fit for

the storage modulus does not describe our data well in Figure 28, it is not surprising to

see that the calculated loss modulus is also off from the data. We therefore conclude that

the linear viscoelastic model fails to apply to our data.
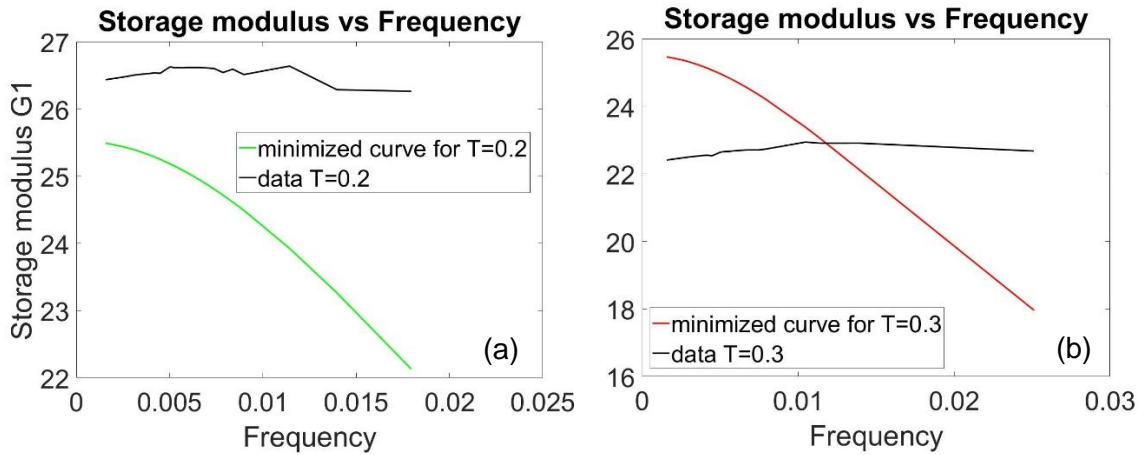
Figure 28: Attempt for fitting the storage modulus using relations based on the standard

solid model, (a) T=0.2, (b) T=0.3
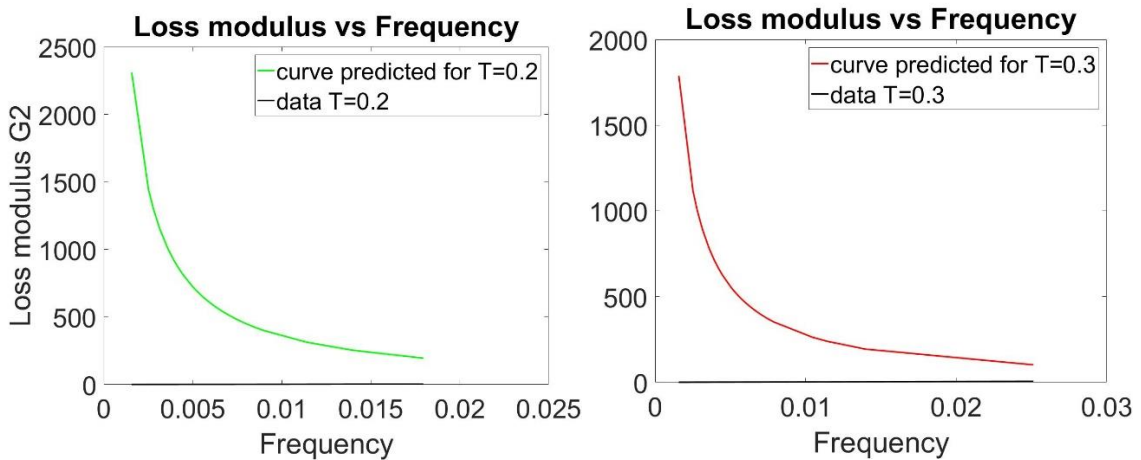
Figure 29: The calculated loss modulus using fitted parameters obtained from storage

modulus calculation by applying the standard solid model, (a) T=0.2, (b) T=0.3

4.4 Future Study Suggestions

From the previous section, the linear viscoelastic model fails to account for our data. We suggest future efforts on re-examining the model for viscoelastic response of ESSs with a lower loading frequency range. This will help identify if the failure is due to our choice of parameters, or if it is the inappropriate model to use for ESSs systems. By doing so will also help understanding the underlying mechanism of the background increase in loss modulus and features of the storage modulus.

5. CONCLUSION

In this study we investigated the viscoelastic response of two-component, defect-free, face-centered cubic ESSs by performing molecular dynamics simulations of cyclic deformation. We found that ESSs exhibit viscoelasticity, where the energy dissipations are loading frequency dependent and atomic misfit dependent. As the distortion in the structure increases, more energy is dissipated within the same loading frequency range. At certain frequencies, we observed resonant vibrations, which lead to peaks in loss modulus-frequency graphs. As the misfit increases, the storage modulus of ESSs decreases and does not obey the rule of mixture. We made an attempt to apply linear viscoelastic model to our result and conclude that the model does not fit our high loading frequency regime.

REFERENCES

1.   M. J. Demkowicz, Plurality of inherent states in equiatomic solid solutions. *Physical Review B* **95**, 094108 (2017).

2.   M. L. Falk, J. S. Langer, Dynamics of viscoplastic deformation in amorphous solids. *Physical Review E* **57**, 7192-7205 (1998).

3.   J. S. Langer, Dynamics of shear-transformation zones in amorphous plasticity: Formulation in terms of an effective disorder temperature. *Physical Review E* **70**, 041502 (2004).

4.   K. P. Menard, *Dynamic mechanical analysis : a practical introduction.* (Boca Raton, Fla. : CRC Press, 2008).

5.   T. Egami, Y. Waseda, Atomic size effect on the formability of metallic glasses. *J. Non·Cryst. Solids* **64**, 113-134 (1984).

6.   M.-H. Tsai, J.-W. Yeh, High-Entropy Alloys: A Critical Review. *Materials Research Letters* **2**, 107-123 (2014).

7.   A. S. Argon, Plastic deformation in metallic glasses. *Acta Metall.* **27**, 47-58 (1979).

8.   A. S. Argon, H. Y. Kuo, Plastic flow in a disordered bubble raft (an analog of a metallic glass). *Materials Science and Engineering* **39**, 101-109 (1979).

9.   F. H. Stillinger, T. A. Weber, Packing Structures and Transitions in Liquids and Solids. *Science* **225**, 983-989 (1984).

10. F. H. Stillinger, T. A. Weber, Dynamics of structural transitions in liquids. *Phys. Rev. A* **28**, 2408-2416 (1983).

11. J. W. Yeh *et al.*, Nanostructured High-Entropy Alloys with Multiple Principal Elements: Novel Alloy Design Concepts and Outcomes. *Adv. Eng. Mater.* **6**, 299-303 (2004).

12. B. Gludovatz *et al.*, A fracture-resistant high-entropy alloy for cryogenic applications. *Science* **345**, 1153-1158 (2014).

13. Z. Wang *et al.*, The effect of interstitial carbon on the mechanical properties and dislocation substructure evolution in Fe40.4Ni11.3Mn34.8Al7.5Cr6 high entropy alloys. *Acta Mater.* **120**, 228-239 (2016).

14. N. A. P. K. Kumar, C. Li, K. J. Leonard, H. Bei, S. J. Zinkle, Microstructural stability and mechanical behavior of FeNiMnCr high entropy alloy under ion irradiation. *Acta Mater.* **113**, 230-244 (2016).

15. R. Ranganathan, Y. Shi, P. Keblinski, Frequency-dependent mechanical damping in alloys. *Physical Review B* **95**, 214112 (2017).

16. T. F. Middleton, J. Hernández-Rojas, P. N. Mortenson, D. J. Wales, Crystals of binary Lennard-Jones solids. *Physical Review B* **64**, 184201 (2001).

17. W. Kob, H. C. Andersen, Testing mode-coupling theory for a supercooled binary Lennard-Jones mixture I: The van Hove correlation function. *Physical Review E* **51**, 4626-4641 (1995).

18. F. Sciortino, W. Kob, P. Tartaglia, Inherent Structure Entropy of Supercooled Liquids. *Phys. Rev. Lett.* **83**, 3214-3217 (1999).

19. R. Goetz, R. Lipowsky, Computer simulations of bilayer membranes: Self-assembly and interfacial tension. *The Journal of Chemical Physics* **108**, 7397-7409 (1998).

20. S. Swayamjyoti, J. F. Löffler, P. M. Derlet, Local structural excitations in model glasses. *Physical Review B* **89**, 224201 (2014).

21. M. P. Allen, D. J. Tildesley, *Computer simulation of liquids. Second edition. Michael P. Allen, Dominic J. Tildesley.* (Oxford ; New York : Oxford University Press, 2017. Second edition., 2017).

22. S. Plimpton, Fast Parallel Algorithms for Short-Range Molecular Dynamics. *J. Comput. Phys.* **117**, 1-19 (1995).

23. T. Schnabel, J. Vrabec, H. Hasse, Unlike Lennard–Jones parameters for vapor–liquid equilibria. *J. Mol. Liq.* **135**, 170-178 (2007).

24. G. Wahnström, Molecular-dynamics study of a supercooled two-component Lennard-Jones system. *Phys. Rev. A* **44**, 3752-3764 (1991).

25. L. Xie, P. Brault, A.-L. Thomann, J.-M. Bauchire, AlCoCrCuFeNi high entropy alloy cluster growth and annealing on silicon: A classical molecular dynamics simulation study. *Appl. Surf. Sci.* **285**, 810-816 (2013).

26. R. M. Ernst, S. R. Nagel, G. S. Grest, Search for a correlation length in a simulation of the glass transition. *Physical Review B* **43**, 8070-8080 (1991).

27. R. J. Good, C. J. Hope, New Combining Rule for Intermolecular Distances in Intermolecular Potential Functions. *The Journal of Chemical Physics* **53**, 540-543 (1970).

28.	J. Delhommelle, P. MilliÉ, Inadequacy of the Lorentz-Berthelot combining rules for accurate predictions of equilibrium properties by molecular simulation. *Mol. Phys.* **99**, 619-625 (2001).

29.	L. Ju, AtomEye: an efficient atomistic configuration viewer. *Modell. Simul. Mater. Sci. Eng.* **11**, 173 (2003).

30.	J. R. Taylor, *Classical mechanics. John R. Taylor*. (Sausalito, Calif. : University Science Books, ©2005., 2005).

31.	S. Toxvaerd, J. C. Dyre, Communication: Shifted forces in molecular dynamics. *The Journal of Chemical Physics* **134**, 081102 (2011).

32.	D. P. Bertsekas, *Nonlinear programming. 2nd ed. Dimitri P. Bertsekas*. (Belmont, Mass. : Athena Scientific, 2nd ed., 1999).

33.	E. T. Mark, A. José, L.-R. Roberto, L. J. Andrea, J. M. Glenn, A Liouville-operator derived measure-preserving integrator for molecular dynamics simulations in the isothermal–isobaric ensemble. *J. Phys. A: Math. Gen.* **39**, 5629 (2006).

34.	M. J. Demkowicz, Viscoelasticity. MSEN 625, Lecture 6 (2016)

APPENDIX

Table 2: List of MD times after each increment and the corresponding loading frequencies

#	MD Time after each increment	Loading Frequency	#	MD Time after each increment	Loading Frequency
1	12500	1.00531E-05	24	30	0.004189
2	10000	1.25664E-05	25	8	0.015708
3	8000	1.5708E-05	26	25	0.005027
4	6250	2.01062E-05	27	24	0.005236
5	5000	2.51327E-05	28	23	0.005464
6	4000	3.14159E-05	29	22	0.005712
7	2500	5.02655E-05	30	21	0.005984
8	2000	6.28319E-05	31	20	0.006283
9	1250	0.000100531	32	19	0.006614
10	1000	0.000125664	33	18	0.006981
11	800	0.00015708	34	17	0.007392
12	500	0.000251327	35	16	0.007854
13	400	0.000314159	36	15	0.008378
14	250	0.000502655	37	14	0.008976
15	200	0.000628319	38	13	0.009666
16	125	0.00100531	39	12	0.010472
17	100	0.001256637	40	11	0.011424
18	80	0.001570796	41	10	0.012566
19	50	0.002513274	42	9	0.013963
20	45	0.002792527	43	8	0.015708
21	40	0.003141593	44	7	0.017952
22	35	0.003590392	45	6	0.020944
23	32	0.003926991	46	5	0.025133